

Meandering Microstrip Leaky Wave Antenna With Dual-Band Linear–Circular Polarization and Suppressed Open Stopband

Pratik Vadher^{ID}, *Student Member, IEEE*, Giulia Sacco^{ID}, *Member, IEEE*,
and Denys Nikolayev^{ID}, *Senior Member, IEEE*

Abstract—This article proposes a dual-band frequency scanning meandering microstrip leaky wave antenna with linear polarization in the Ku-band and circular polarization in the K-band. This is achieved by making use of two spatial harmonics for radiation. The unit cell of the periodic microstrip antenna contains three meanders with mitred corners. To ensure circular polarization, a theoretical formulation is developed taking into account the delay caused by the microstrip length intervals. It defines the unit cell geometry by determining the length of the meanders to ensure that the axial ratio remains below 3 dB throughout the operational band. Moreover, the meanders are used to provide better control over scanning rate (the ratio of change in angle of maximum radiation with frequency) and reduce spurious radiation of harmonics by ensuring single-harmonic operation within the operational band. To guarantee continuous scanning through broadside direction, open stopband is suppressed using mitered angles. The antenna is designed on a 0.254-mm substrate making it suitable for conformal applications. The fabricated antenna shows a backward-to-forward beam steering range of 72° (−42° to 30°) in the K-band (19.4–27.5 GHz) with circular polarization and of 75° (−15° to 60°) in the Ku-band (11–15.5 GHz) with linear polarization.

Index Terms—Higher spatial order, K-band, Ku-band, leaky wave antenna (LWA), meandering microstrip antenna, scanning rate.

I. INTRODUCTION

PERIODIC leaky wave antennas (LWAs) are a class of traveling-wave antennas that radiate energy at the discontinuities of the guiding medium [1]. The changes in frequency cause dispersion within the guiding medium, resulting in varying excitation phases at the discontinuities. This, in turn, alters the main beam pointing direction in the radiation pattern of the antenna with respect to frequency. One-dimensional

Manuscript received 25 April 2023; revised 3 October 2023; accepted 21 October 2023. Date of publication 6 November 2023; date of current version 9 February 2024. This work was supported in part by the French Agence Nationale de la Recherche (ANR) through the Project MedWave under Grant ANR-21-CE19-0045, in part by the European Union's Horizon 2020 Research and Innovation Program under Grant N°899546 (Marie Skłodowska-Curie REACH-IT project), and in part by the European Union's Horizon Europe Research and Innovation Program under Grant N°101063966 (Marie Skłodowska-Curie IN-SIGHT project). (Corresponding author: Denys Nikolayev.)

The authors are with the CNRS, IETR—UMR 6164, University of Rennes, 35000 Rennes, France (e-mail: denys.nikolayev@deniq.com).

Color versions of one or more figures in this article are available at <https://doi.org/10.1109/TAP.2023.3328558>.

Digital Object Identifier 10.1109/TAP.2023.3328558

periodic LWAs (1-D LWAs) typically radiate a fan-beam in the *E*-plane. The direction of maximum radiation changes in the *H*-plane with the change in frequency [2].

Many 1-D periodic LWAs have been proposed using different guiding media. LWAs proposed in [3], [4], [5], [6], and [7] use substrate integrated waveguide (SIW) or half-mode SIW to support the traveling wave and usually use TE_{n0} or in certain cases TM₁₁ mode [8] for radiation. However, to reduce fabrication complexity, lower manufacturing costs, and to enable the creation of compact antennas, microstrip-based guiding media LWAs are an appealing solution [9], [10], [11], [12], [13]. Meandering microstrip LWAs radiate due to the discontinuities created at the edges which results in a net magnetic current responsible for radiation [13], [14].

Since LWAs are periodic structures, infinite spatial harmonics exist in the guiding media [2], [15]. Many SIW-based LWAs that use higher order Floquet modes for radiation have been proposed recently [16], [17]. Although previous works report scanning due to higher spatial harmonics, the scanning is due to two or three spatial harmonics at the same time, which leads to more than one beam radiated by the antenna. However, it is desirable to have a single beam scanning operation over a high scanning range. This is possible when only a single spatial harmonic is responsible for radiation. Hence, better separation of different spatial harmonics is necessary.

To be suitable for on-body conformal applications [18], [19], [20], [21], the antenna must be flexible and bendable [22]. For such a purpose, antennas based on microstrip technology are an excellent candidate. In addition, mechanical properties such as tensile modulus of the dielectric substrate also play an important factor. Hence, the Rogers 3003 substrate ($\epsilon_r = 3.0$) is preferred in this work due to its low tensile modulus (823 MPa) making it flexible.

Moreover, it is desirable to have circular polarization for many different applications where the alignment of the receiving and transmitting antenna may impact the overall performance of the system such as radars [23], satellite communications, and on-body antenna system [21], [24], [25].

The presence of open stopbands (OSBs) also impacts the scanning of the antenna through the broadside direction [26], [27]. Several techniques have been proposed to suppress or completely mitigate OSBs [28], [29], [30]. At the OSB frequency, the input impedance matching is poor and the Bloch

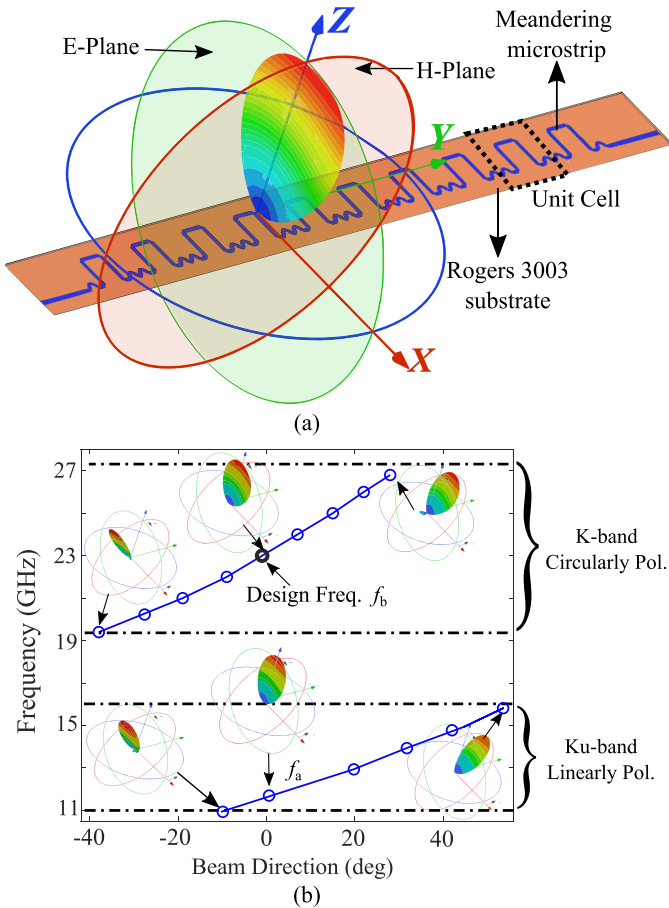


Fig. 1. (a) Configuration of the proposed ten unit cells periodic frequency scanning antenna with radiation pattern shown in the broadside direction. The meandering microstrip is etched on the top layer while the bottom layer is copper. (b) Beam scanning operation of the proposed LWA as a function of frequency in the Ku-band and K-band. The antenna radiates a fan-beam in the E-plane ($X - Z$ plane), while in the H-plane ($Y - Z$ plane) the antenna changes the direction of maximum radiation with change in frequency.

impedance (Z_s) has a high imaginary value. Hence, the aim is to minimize the high imaginary value of impedance to reduce the effects of OSB. The idea of beam scanning due to higher spatial harmonic, limited to a single band and linear polarization, has been presented in [31] with no suppression of OSB.

In this article, single-layer PCB meandering microstrip-based LWA is proposed with dual-band operation without the use of vias shown in Fig 1(a). The Ku-band operation of the antenna is due to the $n = -1$ spatial harmonic and it exhibits linear polarization, while the second band of operation at the K-band is due to $n = -2$ and it depicts circular polarization as described in Fig. 1(b). The unit cell of the periodic antenna consists of three meanders to ensure single-beam operation by providing better separation between different spatial harmonics.

The structure of this article is as follows. Section II details the concept of higher spatial order in a microstrip-based unit cell followed by theoretical formulation for the dimensions required to have circular polarization for a unit cell with single meander. In Section III, the unit cell is modified by adding two smaller meanders to increase the separation of spatial

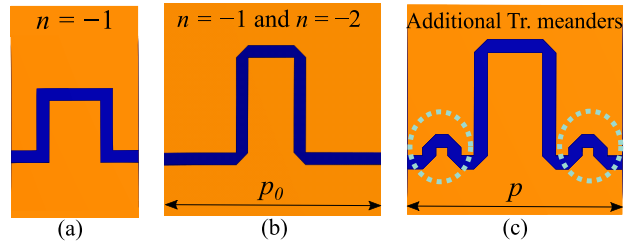


Fig. 2. Evolution toward final design of the proposed unit cell. (a) Conventional unit cell operating in single band and radiating due to the $n = -1$ spatial harmonic, (b) dual-band operating unit cell radiating due to $n = -1$ and $n = -2$ spatial harmonics, and (c) modified unit cell with the introduction of two meanders ($p < p_0$) to improve scanning range and circular polarization performance.

harmonics and ameliorate the performance of circular polarization over the larger frequency operation range. The smaller meanders also result in better control over scanning rate (i.e., the ratio between the change in the angle of maximum radiation and the change in frequency $\Delta\theta/\Delta f$). A technique to remove OSB is discussed using Bloch impedance subsequently. Section IV contains the comparison of simulations and measurements for the final design. In Section V, the conclusions of the study are presented.

II. RADIATION MECHANISM AND PRINCIPLE FOR ANTENNA DESIGN

Fig. 1(a) shows the design of the proposed microstrip-based LWA with mitred corners. As detailed in previous works on microstrip-based LWAs [13], the radiation occurs due to the magnetic current at the corners of the meandering microstrip.

The evolution toward the final design of the unit cell is shown in Fig. 2. Conventional microstrip-based LWA [13], [32], [33], [34] operate in the radiation zone due to spatial harmonic of $n = -1$ like the unit cell shown in Fig. 2(a). This unit cell can be modified to operate in the $n = -2$ spatial harmonic, by increasing the path length at the desired operational frequency. By introducing mitred corners and properly choosing the length of the interconnecting microstrip lines between the corners, the antenna radiates in circular polarization [see Fig. 2(b)]. The unit cell operates in the radiation zone associated with $n = -1$ and $n = -2$ spatial harmonics.

To improve the separation of radiation zone due to two harmonics ($n = -1, -2$), we propose the geometry in Fig. 2(c). The unit cell is modified with two additional meanders resulting in improvement in scanning range and circular polarization. The antenna has been optimized for operation in the circularly polarized K-band using the spatial harmonic of $n = -2$, and all the theoretical formulations for the unit cell dimensions have been performed to ensure optimal performance in this frequency range.

A. Higher Order Spatial Harmonics in the Unit Cell Based on Microstrip Design

Fig. 3(c) shows the microstrip-based unit cell with single meander with four radiating elements due to four mitred corners. Due to the periodicity (p_0) of the structure, infinite

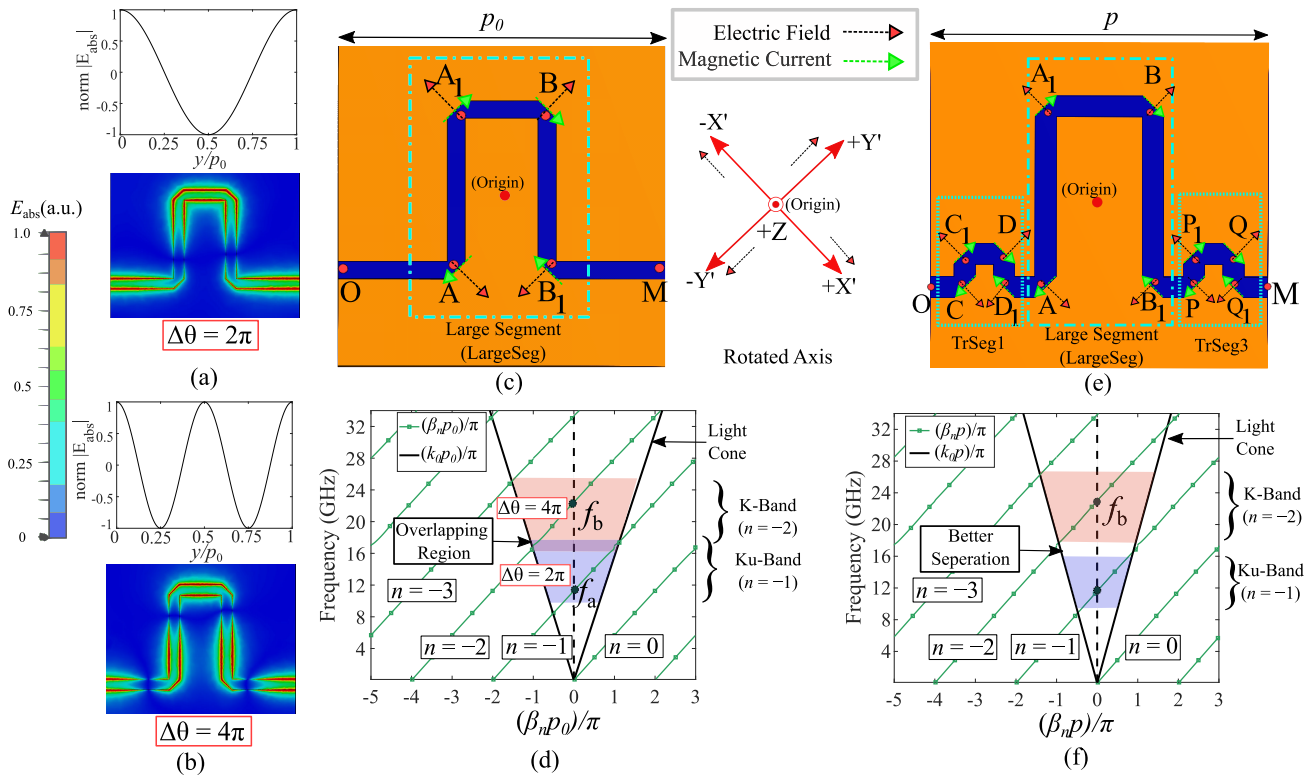


Fig. 3. E_{abs} plots at phase 0° for the frequency at which broadside radiation occurs for (a) $n = -1$ and (b) $n = -2$. The sinusoidal graphs above E_{abs} plots are representative of the electric field variation across microstrip line throughout the unit cell. (c) Unit cell with single large meander. Radiation sources for a single large meander are depicted in the figure. The four radiating magnetic current sources are shown at points A, A₁, B, and B₁. (d) Brillouin diagram for the unit cell with the single meander. (e) Unit cell design with two additional meanders that results in 12 radiation sources. (f) Brillouin diagram for the improved unit cell with two additional meanders.

number of space harmonics exist due to the Bloch–Floquet theorem [35], [36]. The phase constant of the n^{th} space harmonic β_n satisfies

$$\beta_n p_0 = \beta_0 p_0 + 2n\pi \quad (1)$$

where n ranges from $-\infty$ to $+\infty$. Here, β_0 is the zeroth-order spatial harmonic of periodic LWA

Fig. 3(d) shows the corresponding Brillouin diagram for the unit cell. The n^{th} spatial harmonic inside the light cone ($|\beta_n| < |k_0|$) results in radiation [15]. It is to be noted that multiple spatial harmonics can exist within the light cone resulting in multiple beam radiation [16].

The phase difference across the unit cell for the first two higher harmonics $n = -1$ and $n = -2$ can be described from (1) with respect to fundamental harmonic.

Consequently, the direction of maximum radiation θ_n corresponding to the n^{th} spatial harmonic is given by [16], [36], and [37]

$$\theta_n = \sin^{-1}(\beta_{-n} p_0 / k_0 p_0) \quad (2)$$

where k_0 is the free-space wavenumber.

According to (2), when the phase difference across the unit cell ($\beta_{-n} p_0$) is zero, the direction of the main beam of the n^{th} spatial harmonic is in the broadside direction. Hence, at the frequencies of broadside radiation for spatial harmonics $n = -1$ and $n = -2$, the phase difference across the unit cell

with periodicity p_0 from (1) is

$$\beta_{-1} p_0|_{f=f_a} = 0 \rightarrow \beta_0 p_0|_{f=f_a} = 2\pi \quad (3a)$$

$$\beta_{-2} p_0|_{f=f_b} = 0 \rightarrow \beta_0 p_0|_{f=f_b} = 4\pi \quad (3b)$$

where f_a and f_b are the frequencies corresponding to the broadside radiation for $n = -1$ and $n = -2$, respectively. Fig. 3(a) and (b) depicts the variation in electric field magnitude at the two frequencies confirming the above two equations. To summarize, the first Ku-band radiation is due to spatial harmonic $n = -1$, while the second K-band radiation is due to spatial harmonic $n = -2$.

Equation (3b) implies that at $f = f_b$, the total phase difference (ϕ_{p_0}) across the unit cell is equal to 4π . Therefore, the equation to have broadside radiation for second harmonic at the design frequency $f = f_b$ is

$$4\pi = \phi_{OA_1|f=f_b} + \phi_{AA_1|f=f_b} + \phi_{A_1B|f=f_b} + \phi_{BB_1|f=f_b} + \phi_{B_1M|f=f_b}. \quad (4)$$

Here, ϕ_{ij} is the phase difference across the line segment between the points i and j , where $i, j \in \{A, A_1, B, B_1, O, M\}$. As indicated earlier, the reason for designing the antenna for the second harmonic is to obtain dual-band operation due to spatial harmonics $n = -1$ and $n = -2$.

B. Analysis for Circular Polarization in the Radiation Zone for Spatial Harmonic $n = -2$

To analyze the circular polarization easily, the axis is rotated equal to the angle of mitred corners as shown in Fig. 3(c). Hence, there are two transverse components ($E_{X'}$ and $E_{Y'}$) radiating from the mitred corners.

The ratio of the two transverse fields $E_{X'}$ and $E_{Y'}$, in the X' and Y' direction, respectively [14],

$$\frac{E_{Y'}}{E_{X'}} = e^{j(\phi_{AA_1} + \phi_{A_1B})}. \quad (5)$$

To have the circular polarization, the two transverse components of electric field ($E_{X'}$ and $E_{Y'}$) need to have a phase difference of odd multiple of $\pi/2$ [2]. Consequently, the condition to obtain circular polarization for a traveling-wave meandering microstrip antenna is stated by [14]

$$\phi_{AA_1} + \phi_{A_1B} = (2k + 1)\pi/2 \quad (6)$$

where $k = 1, 2, \dots$.

Since the desire is to operate in spatial harmonic $n = -2$, from (3b), the conclusion can be made to select $k = 1$, hence

$$\phi_{AA_1} + \phi_{A_1B} = 3\pi/2. \quad (7)$$

Selecting $k \geq 2$ would lead to similar result with (5) still being satisfied; however, this would increase the overall period of the unit cell resulting in undesirable harmonics in the radiation zone.

Equation (7) imposes a criterion on the phase difference and hence the length of microstrip interval between two corners A and B for achieving circular polarization. In addition, the length of the line segment between the points i and j , indicated earlier, is represented by l_{ij} . To have accurate length of line intervals, the model from [9] is chosen for analysis. For initial dimensions, at the design frequency $f = f_b$, l_{AA_1} is taken such that $\phi_{AA_1} = \pi$. This implies that $\phi_{A_1B} = \pi/2$.

From Fig. 3(d), $l_{AA_1} = l_{BB_1}$ which implies $\phi_{AA_1} = \phi_{BB_1}$. Also, the unit cell is considered symmetric, hence $l_{OA} = l_{B_1M}$.

The phase difference across the large meander (consisting of AA_1 , A_1B , and BB_1) is defined as $\phi_{LargeSeg}$. Therefore, from (7), to have the best circular polarization performance at the desired design frequency of $f = f_b$

$$\begin{aligned} \phi_{LargeSeg}|_{f=f_b} &= \phi_{AA_1}|_{f=f_b} + \phi_{A_1B}|_{f=f_b} + \phi_{BB_1}|_{f=f_b} \\ &= 5\pi/2. \end{aligned} \quad (8)$$

Consequently, there are two design constraints on the length of microstrip line intervals as follows.

- 1) Equation (4), to construct a unit cell that has broadside radiation at $f = f_b$.
- 2) Equation (8), to construct a unit cell with best circular polarization performance at $f = f_b$.

Table I depicts the dimensions of the unit cell based on the theory discussed at $f_b = 23$ GHz. The dimensions are mentioned in the form of λ_b , corresponding wavelength to frequency f_b in the microstrip medium.

The dielectric is chosen as Rogers 3003 ($\epsilon_r = 3.0$) while the height of the substrate is $h_{sub} = 0.254$ mm. The width of the microstrip t_{50} is equal to 0.5 mm. It is important to

TABLE I
DIMENSIONS OF THE UNIT CELL DESIGNED TO OPERATE IN THE $n = -2$ SPATIAL HARMONIC AND HAVE CIRCULARLY POLARIZED FIELDS. HERE NOTE THAT λ_b IS THE CORRESPONDING WAVELENGTH IN THE MICROSTRIP MEDIUM AT $f = f_b$

Line interval	Expressed in λ_b	Phase diff. across line interval	Physical dim. (mm)
OA	$3\lambda_b/8$	$3\pi/4$	3.21
AA ₁	$\lambda_b/2$	π	4.44
A ₁ B	$\lambda_b/4$	$\pi/2$	2.47
BB ₁	$\lambda_b/2$	π	4.44
B ₁ M	$3\lambda_b/8$	$3\pi/4$	3.21
p_0	-	4π	5.8
t_{50}	-	-	0.5
h_{sub}	-	-	0.254

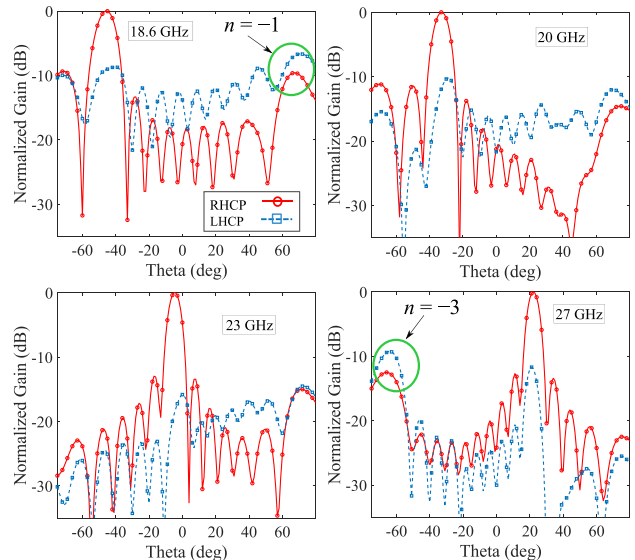


Fig. 4. Normalized RHCP and LHCP gains in the H plane obtained from simulation for the LWA formed by connecting ten unit cells with singular meander. The main lobe is due to the spatial harmonic of $n = -2$. The realized gain of the main lobe varies from 8 dB to 14 dB across the frequency range.

note that in the microstrip medium, the effective $\epsilon_{r,eff}(f = 0)$ is 2.375 calculated from [38]. To account for the dispersive nature of microstrip media, the model proposed by Pramanick and Bhartia from [39] is considered to calculate $\epsilon_{r,eff}(f = f_b)$. These parameters are taken into consideration when calculating λ_b in the microstrip medium.

Ten such unit cells with single meander are cascaded next to each other to form a LWA, and full-wave simulations are performed in Computer Simulation Technology (CST) Studio Site and ANSYS High Frequency Structure Simulator (HFSS). Fig. 4 shows the radiation pattern indicating the beam scanning with frequency and circular polarization nature of the antenna. As can be seen, at lower end of frequency range $f = 18.6$ GHz, there is another beam of spatial harmonic of $n = -1$ limiting the scanning.

The corresponding axial ratio obtained through simulation at the angle of maximum gain is shown in Fig. 5(a). The antenna has good circular polarization performance near the design frequency of $f_b = 23$ GHz. The frequency range where

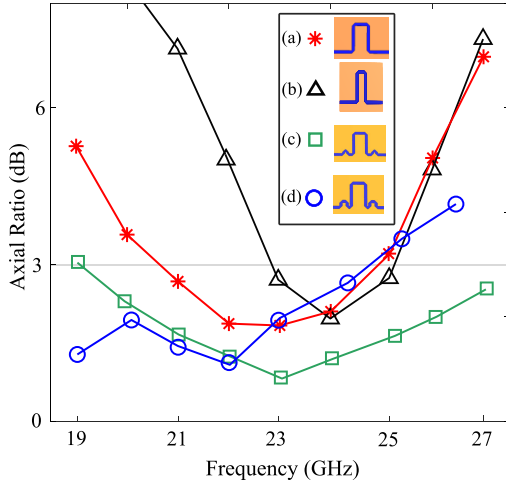


Fig. 5. Axial ratio values in the main beam direction versus frequency obtained by full-wave simulation of ten unit cells connected in series for three cases. (a) Single meander with $\phi_{AA_1} = \pi$ and (b) single meander with $\phi_{AA_1} = 9\pi/8$ to reduce the period of the unit cell and in the presence of two additional meanders on either side of large meander (with $\phi_{AA_1} = \pi$) with the size (c) ($\phi_{sect} = 10^\circ$) and (d) ($\phi_{sect} = 25^\circ$).

the axial ratio is lower than 3 dB is from 20 to 25.2 GHz with the beam scanning from $(-26^\circ$ to $+10^\circ$).

C. Improvement in the Scanning Range by Reducing the Period of the Unit Cell

In the previous subsection, initial dimensions were taken such that $\phi_{AA_1} = \pi$ and $\phi_{A_1B} = \pi/2$ at $f = f_b$. The scanning range and the separation of the harmonics can be increased by reducing the period of a unit cell. If the vertical length l_{AA_1} is increased such that $\phi_{AA_1} = 9\pi/8$, then according to (7), to maintain the circular polarization performance $\phi_{A_1B} = \pi/4$ at the design frequency f_b . This reduces the period of the unit cell since the horizontal interval (l_{A_1B}) of the unit cell is shortened leading to better separation of harmonics. The rest of the dimensions remain the same as discussed in Table I.

Ten such unit cells are connected in series to form a LWA and full-wave simulations are performed in CST and Ansys HFSS. This results in an increase in the scanning rate (the change in β with the change in frequency) as can be seen in Fig. 6(a) and (b). However, as shown in Fig. 5(b), there is a negative impact on the circular polarization performance in the operating frequency band.

In both, the discussed cases with only a single meander in the unit cell [see Fig. 5(a) and (b)], at the design frequency $f = f_b$ and in the frequency range close to it, the antenna shows good circular polarization performance. However, it deteriorates quite fast toward the lower and higher ends of the band. Hence, the beam scanning range is pretty limited.

It can be concluded that using a unit cell with only a single large meander is extremely challenging and may not be feasible to obtain large beam scanning range with good circular polarization performance.

III. IMPROVEMENT IN THE SCANNING RANGE AND CIRCULAR POLARIZATION BY ADDITIONAL MEANDERS

To enhance the beam steering range, improve circular polarization performance across the operational frequency band

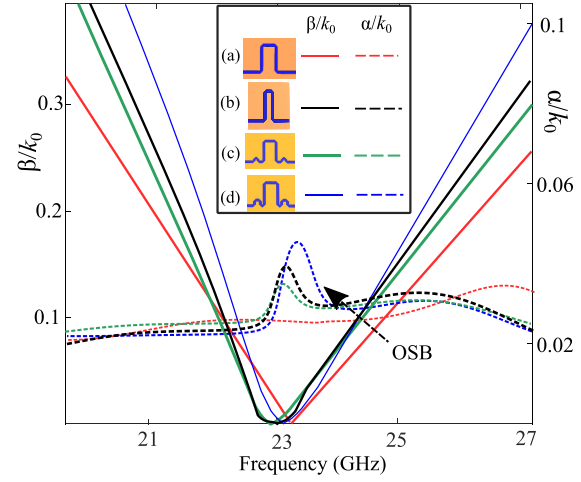


Fig. 6. Change in the dispersion parameters (β and α) for four cases. (a) Single meander with $\phi_{AA_1} = \pi$. (b) Single meander with $\phi_{AA_1} = 9\pi/8$ to reduce the period of the unit cell, in the presence of two additional meanders on either side of large meander ($\phi_{AA_1} = \pi$) with the size of (c) ($\phi_{sect} = 10^\circ$) and (d) ($\phi_{sect} = 25^\circ$). OSB expands with the increase in size of additional meanders.

and gain better control over scanning rate ($\Delta\theta/\Delta f$), two additional smaller meanders are introduced on either side of larger meander at an equal distance from the center of the unit cell. The following sections describe the characteristics and steps to design such a unit cell.

A. Constructing the Unit Cell With Three Meanders for Dual-Band Operation

Fig. 3(e) depicts the design of improved unit cell. The first additional meander consists of three microstrip line intervals CC_1 , C_1D , and DD_1 , while the third additional meander consists of line intervals PP_1 , P_1Q , and QQ_1 . The length of each of these six microstrip line intervals is equal. The phase difference across each of these microstrip line intervals is defined to be ϕ_{sect} . In addition, the phase difference due to the first and third meanders is denoted by ϕ_{TrSeg1} and ϕ_{TrSeg3} , respectively.

The unit cell is designed to be symmetric, and therefore, the phase difference across the line intervals is $\phi_{D_1A} = \phi_{B_1P}$, $\phi_{OC} = \phi_{Q_1M}$, and $\phi_{TrSeg1} = \phi_{TrSeg3}$. Furthermore, the phase difference across the first meander and the third meander can be written as

$$\phi_{TrSeg1} = \phi_{CC_1} + \phi_{C_1D} + \phi_{DD_1} = 3 \times \phi_{sect} \quad (9a)$$

$$\phi_{TrSeg3} = \phi_{PP_1} + \phi_{P_1Q} + \phi_{QQ_1} = 3 \times \phi_{sect}. \quad (9b)$$

To have broadside radiation at $f = f_b$, a 4π phase difference across the unit cell period p must be satisfied. Consequently, from the Fig. 3(e), the design equation for the improved unit cell can be written as

$$4\pi = \phi_{OC|f=f_b} + \phi_{TrSeg1|f=f_b} + \phi_{D_1A|f=f_b} + \phi_{LargeSeg|f=f_b} + \phi_{B_1P|f=f_b} + \phi_{TrSeg3|f=f_b} + \phi_{Q_1M|f=f_b}. \quad (10)$$

Here, ϕ_{ij} represents the phase difference between the points i and j where $i, j \in \{C, C_1, D, D_1, A, A_1, B, B_1, P, P_1, Q, Q_1, O, M\}$.

To maintain circular polarization, it is necessary that the phase difference across larger meander $\phi_{\text{LargeSeg}|f=f_b}$ equals $5\pi/2$, as stated in (8). Therefore, the following design constraint can be derived from (10):

$$6 \times \phi_{\text{sect}|f=f_b} + 2 \times \phi_{D_1A|f=f_b} + 2 \times \phi_{OC|f=f_b} = 3\pi/2. \quad (11)$$

B. Circular Polarization Analysis for the Improved Unit Cell

It was proved in Section II that a single meander unit with four radiating elements can produce circular polarization at the desired design frequency. Hence, for the improved unit cell with 12 radiating currents [see Fig. 3(e)], circular polarization at $f = f_b$ can be achieved if the effect due to radiating currents on the first additional meander (at C, C₁, D and D₁) and the third additional meander (at P, P₁, Q and Q₁) is reduced. This is possible if the direction of current at C is opposite to the current at P resulting in opposing fields at these corners.

The magnetic currents at the corners C and P are oriented along the Y'-axis as shown in Fig. 1(b), but depending on the phase shift introduced by the interconnecting microstrip lines, they can have the same or opposite directions. Hence, the length of the microstrip line intervals in between these two corners can be optimized in such a way that the magnetic currents are in opposite direction at design frequency $f = f_b$.

The direction of magnetic current at C will be opposite to the magnetic current at P if the following constraint is met at $f = f_b$ (since $e^{3\pi} = -1$):

$$\phi_{OP} - \phi_{OC} = 3\pi \quad (12a)$$

$$\phi_{TrSeg1} + \phi_{D_1A} + \phi_{LargeSeg} + \phi_{B_1P} = 3\pi. \quad (12b)$$

From (8), it is known that to maintain circular polarization at $f = f_b$, $\phi_{\text{LargeSeg}} = 5\pi/2$, hence the following design equation is obtained:

$$3 \times \phi_{\text{sect}|f=f_b} + 2 \times \phi_{D_1A|f=f_b} = \pi/2. \quad (13)$$

Equations (8), (11) and (13) are the design constraints on the length of line intervals for the proposed unit cell to maintain broadside radiation and circular polarization at $f = f_b$.

From (8), it is clear that the dimensions for larger meander are fixed to maintain circular polarization. The other dimensions are governed by (11) and (13). This results in three variables (namely, $\phi_{\text{sect}|f=f_b}$, $\phi_{D_1A|f=f_b}$, and $\phi_{OC|f=f_b}$) and two equations. In the current analysis, $\phi_{\text{sect}|f=f_b}$ is considered an independent variable making the other two variables ($\phi_{D_1A|f=f_b}$ and $\phi_{OC|f=f_b}$) dependent. The initial design is chosen such that $\phi_{\text{sect}|f=f_b} = 10^\circ$. The other two dimensional can hence be calculated from (11) and (13). The initial lengths of the microstrip sections following this theory are shown in Table II for $f_b = 23$ GHz. Furthermore, the placements of small meanders with respect to large meander within the unit cell can be varied as well to obtain better circular polarization.

Fig. 8 shows the full-wave simulation of the unit cell at $f = f_b$ designed according to the equations above. As can be seen, the direction of fields at each of the corners in the first smaller meander is opposite to the field at the corresponding corner of the third smaller meander.

Ten such unit cells are sequentially connected as shown in Fig. 1(b) to form a LWA and then simulated in CST. Fig. 5(c)

TABLE II
DIMENSIONS OF THE UNIT CELL WITH THREE MEANDERS DESIGNED
TO OPERATE IN SPATIAL HARMONIC OF $n = -2$ AND HAVE
CIRCULARLY POLARIZED FIELDS. NOTE THAT λ_b IS
WAVELENGTH CORRESPONDING TO f_b
IN MICROSTRIP MEDIUM

Line interval	Initial Values (From the theory)		Optimised (mm)
	Expressed in λ_b	(mm)	
CC ₁ =C ₁ D=DD ₁	$\phi_{\text{sect}} \times (\lambda_b/2\pi)$	0.71	0.745
D ₁ A=B ₁ P	$(\pi/2 - 3\phi_{\text{sect}})/2 \times (\lambda_b/2\pi)$	1.128	1.172
AA ₁	$\lambda_b/2$	4.265	4.343
A ₁ B	$\lambda_b/4$	2.383	3.062
BB ₁	$\lambda_b/2$	4.265	4.343
PP ₁ =P ₁ Q=QQ ₁	$\phi_{\text{sect}} \times (\lambda_b/2\pi)$	0.71	0.745
OC=Q ₁ M	$(\pi - 3\phi_{\text{sect}})/2 \times (\lambda_b/2\pi)$	1.819	0.376
p	-	9.694	8.028
t_{50}	-	0.5	0.5
h_{sub}	-	0.254	0.254

shows the unit cell (in the inset) designed by the formulated theory described above and the simulation, respectively, of the axial ratio obtained for different frequencies over the scanning range for the main fan beam direction emanated from the LWA. Notable improvement in axial ratio performance over a larger frequency band can be observed following the inclusion of two smaller meanders.

C. Improvement in Scanning Range and Better Control of Scanning Rate

The size of the two additional meanders can be changed to modify the period (p) of the unit cell. Fig. 6(a), (c) and (d) shows the impact of the introduction and size of additional meanders on the dispersion parameters α and β_{-2} (radiating harmonic). As can be observed, the slope of β_{-2} as a function of frequency (and hence the beam scanning range of the LWA) can be controlled efficiently by introducing and varying the size of additional meanders.

In Fig. 5(a), (c), and (d), the impact on circular polarization due to alterations in meander size can be observed across a wide range of frequencies in the K-band. The circular polarization at the design frequency f_b remains intact. Increasing the meander size increases the scanning rate ($\Delta\beta_{-2}/\Delta f$); however, the circular polarization over the large band of operation (K-band) is impacted negatively. Hence, in the fabricated prototype the size of small meander corresponding to $\phi_{\text{sect}} = 10^\circ$ is chosen.

D. Overall Performance Improvement Due to the Two Additional Meanders

Due to the two additional smaller meanders, the electrical length of the unit cell has been increased. This results in the following improvements for frequency scanning.

- 1) Enhanced scanning range.
- 2) Better control over scanning rate by dictating the size of path length in the unit cell by reducing or increasing the size of small meanders (ϕ_{sect}).

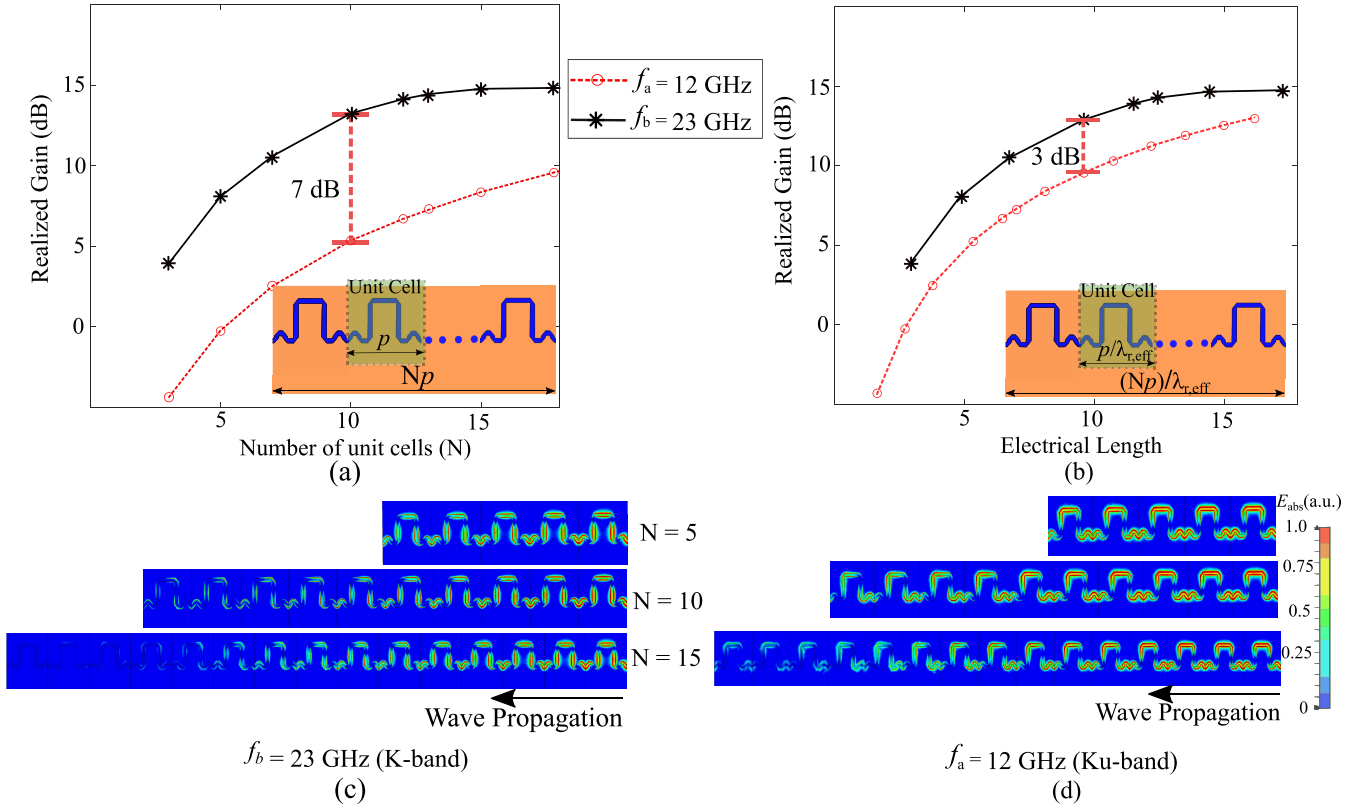


Fig. 7. Increase in the maximum realized gain at $f_a = 12 \text{ GHz}$ and $f_b = 23 \text{ GHz}$ with the increase in (a) physical length and (b) electrical length. Magnitude of electric field along the LWA at (c) $f = f_b$ and (d) $f = f_a$.

- 3) Better separation of spatial harmonics resulting in lower spurious radiation due to undesired spatial harmonics.
- 4) Improvement of circular polarization performance across the band.

By comparing the Brillouin diagrams in Fig. 3(c) and (e) for the unit cell geometry containing one meander and three meanders, respectively, the first three conclusions can be easily drawn. With the help of additional two meanders, the rate of dispersion with frequency is controlled within the unit cell. The impact of the proposed geometry on the circular polarization can be observed from Fig. 5. The acceptable range for frequency scanning (frequency range where axial ratio $< 3 \text{ dB}$) has increased from 20 to 25.2 to 19.4 to 27.5 GHz resulting in an increase in beam steering from $(-26^\circ \text{ to } +10^\circ)$ to $(-42^\circ \text{ to } +30^\circ)$. The beam steering $(-42^\circ \text{ to } +30^\circ)$ is discussed in Section IV.

E. Determining the Number of Unit Cells for LWA

To keep the antenna design compact, determining the length of the LWA ($=Np$) such that it radiates most of the power for the least number of unit cells (N) is quite important. Fig. 7(a) shows the change in gain as a function of the number of unit cells at the design frequency $f_b = 23 \text{ GHz}$. The rate of gain change decreases as the number of unit cells exceeds 10. The plot of electric field magnitude along the antenna [Fig. 7(c)] shows that the antenna radiates most of the power when $N = 10$.

Likewise, the magnitude of electric field at $f_a = 12 \text{ GHz}$ (broadside frequency in the Ku-band) is shown in Fig. 7(d).

For f_a , there is high residual power at the output port when only ten unit cells are cascaded to form LWA. The antenna is electrically smaller in the Ku-band than in the K-band, thus leading to a higher gain in the K-band. The difference in gain is close to 7 dB [Fig. 7(a)].

However, as shown in Fig. 7(b), the gain difference is less than 3 dB between the Ku-band and the K-band of operation when equal electrical length is considered. The electrical length of the LWA is equal to $Np/\lambda_{r,\text{eff}}$, where $\lambda_{r,\text{eff}}$ is the corresponding wavelength in the microstrip medium at f_a and f_b , respectively. Since the antenna in this work is optimized to operate in the K-band, only ten unit cells are cascaded in the designed prototype.

F. Mitigation of OSB

Periodic structures such as LWAs have a frequency band near the broadside frequency (f_b in current case), where there is no conduction of the traveling wave, known as OSB [2], [15]. To remove OSB, the parameter of Bloch impedance (Z_s) has to be analyzed. The Bloch impedance can be calculated from the S-parameters extracted from driven-mode full-wave simulation in terms of circuit parameters A, B, C, and D as shown in [38]

$$Z_s = \frac{-2 \times B}{(A - D - \sqrt{(A + D)^2 - 4})}. \quad (14)$$

Fig. 9 shows the Bloch impedance extracted for the K-band operation range. For the case when OSB is present, at the broadside frequency, $f_b = 23 \text{ GHz}$, there is an abrupt

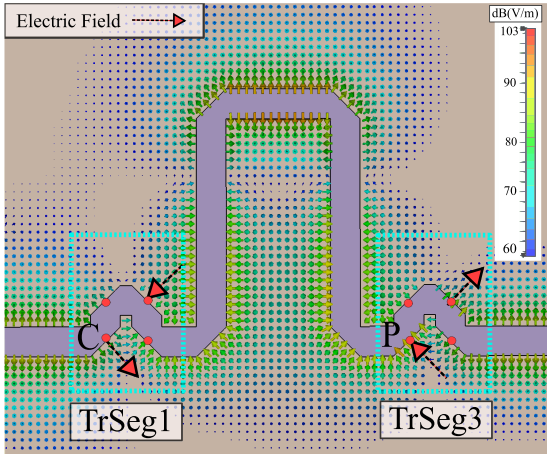


Fig. 8. Full-wave simulation for the unit cell constructed using the theoretical formulation. At $f = f_b$, the electric fields at each of the four mitred corners of TrSeg1 cancel out with the corresponding mitred corner of TrSeg3.

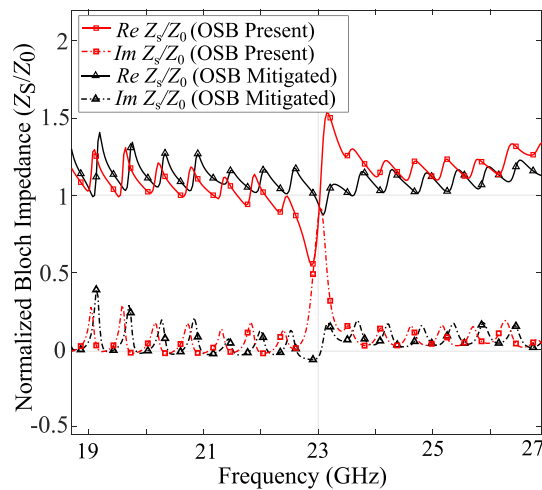


Fig. 9. Bloch impedance of the LWA when OSB is present and when OSB is mitigated by the introduction of additional capacitance. Here, the impedance is normalized to $Z_0 = 50 \Omega$.

increase in imaginary Z_s , which results in poor transmission and high return loss. This results in reduced gain at the broadside region. Furthermore, while OSB is present at $f_a = 12$ GHz and at $f_b = 23$ GHz, its impact is more pronounced at f_b . Hence, more emphasis is placed in the OSB suppression in the K-band.

To mitigate the problem of OSB, a technique similar to [13] is used. For a meandering microstrip with mitred corners, the effect of bending the microstrip line (corners) can be modeled as capacitance [40], [41], [42]. This is clearly evident from Fig. 9 when OSB is present. Hence, the angle for the mitred corners is changed which introduces an additional inductance [41], [42] that reduces the imaginary impedance at $f = f_b$ as shown in Fig. 10. Fig. 9 shows that imaginary impedance goes to zero which leads to mitigation of OSB at broadside direction.

IV. DUAL-BAND LEAKY WAVE ANTENNA

A ten unit cell dual-band LWA, having the layout of Fig. 1(b) and the optimized dimensions listed in Table II, was

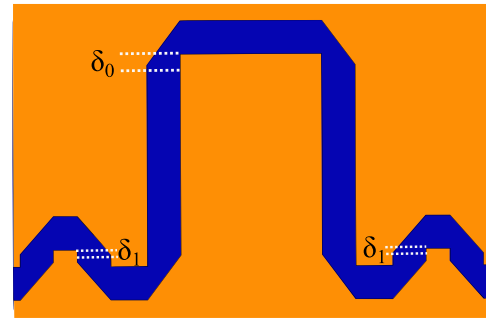


Fig. 10. OSB mitigation by changing the angle of mitred corner. The values of δ_0 and δ_1 are 0.15 and 0.06 mm, respectively.

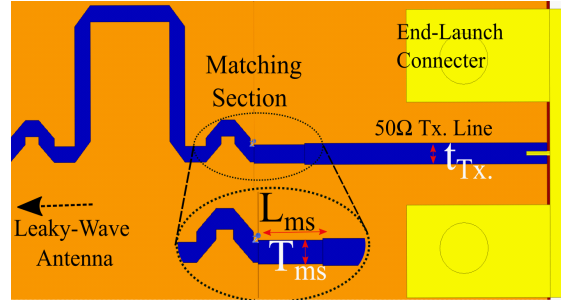


Fig. 11. Feed design to match the output impedance (Z_0) of $50 - \Omega$ connector to input impedance of antenna at around 60Ω . The values for matching section are $T_{ms} = 0.57$ mm and $L_{ms} = 1.634$ mm. The $50 - \Omega$ transmission line is $t_{Tx} = 0.64$ mm.

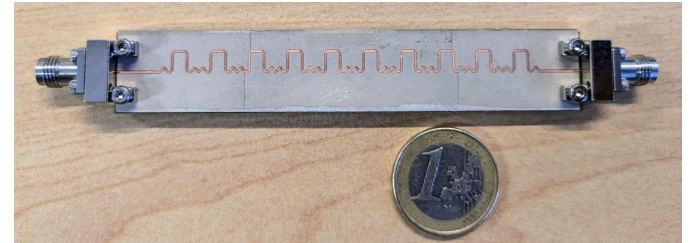


Fig. 12. Fabricated leaky wave antenna.

fabricated. The antenna is based on Rogers 3003 ($\epsilon_r = 3.0$ and $\tan \delta = 0.001$) with a substrate thickness of 0.254 mm.

A. Feed Design

A Bulgin end-launch connector (2.4 mm) with the output impedance $Z_0 = 50 \Omega$ is used to feed the antenna. Z_s of the antenna is around 60Ω throughout the operating frequency range as shown in Fig. 9. Hence, a matching section is added to match the impedance depicted in Fig. 11.

B. Circularly Polarized Radiation in K-Band

In this band, the antenna is right-handed circularly polarized and radiation is due to spatial harmonic of $n = -2$. The measurements are performed at the millimeter-wave test facility CAMILL at Institut d'Électronique et de Télécommunications de Rennes (IETR). The simulated and measured radiation patterns in the azimuth plane are shown in Fig. 13(a) and (d) for the 19.4–27.5 GHz band. The measured radiation pattern at $f = 19.4$ GHz shows higher sidelobes compared with

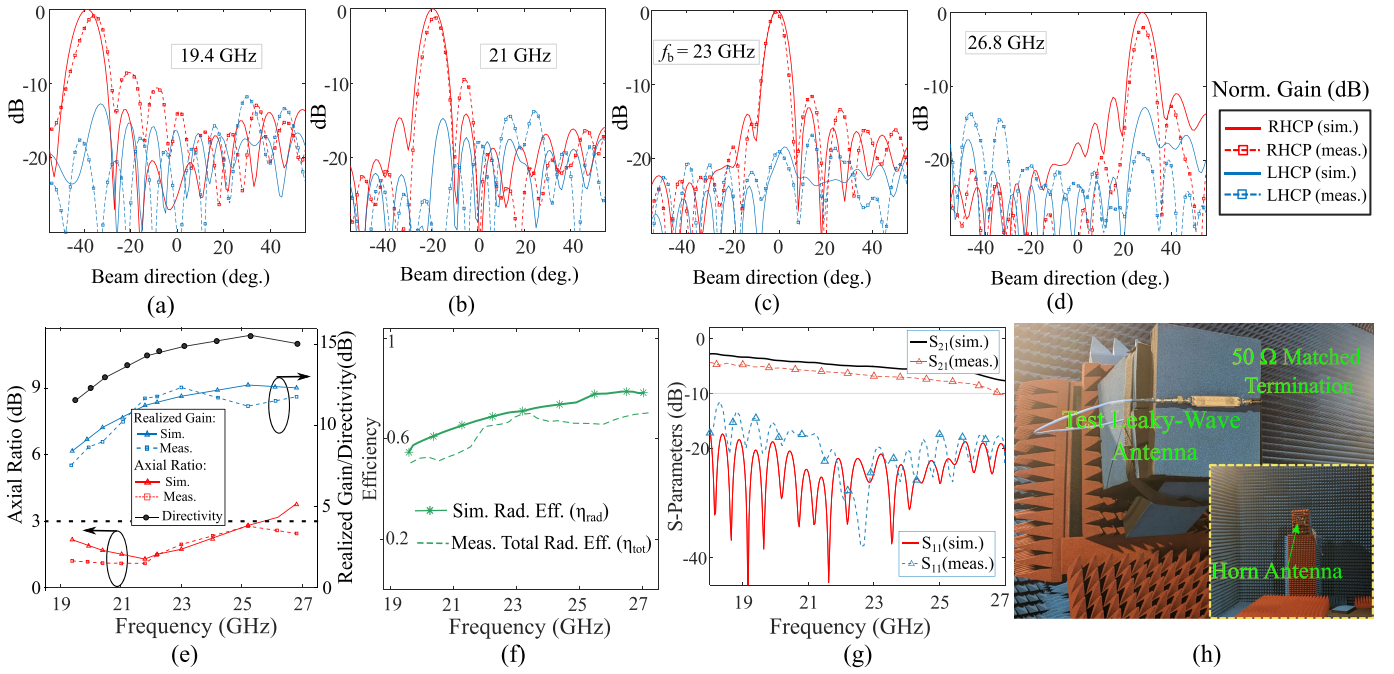


Fig. 13. Measurements in the K-band where the antenna is circularly polarized. Measured and simulated normalized radiation patterns of the fabricated antenna in the H-plane at (a) 19.4, (b) 21, (c) 23 ($= f_b$), and (d) 26.8 GHz. The antenna scans from -42° to 30° in the K-band frequency range. (e) Axial ratio, realized gain, and directivity of the fabricated antenna. (f) Efficiency of the designed antenna. (g) Measured and simulated S -parameters. (h) Measurement setup of the antenna.

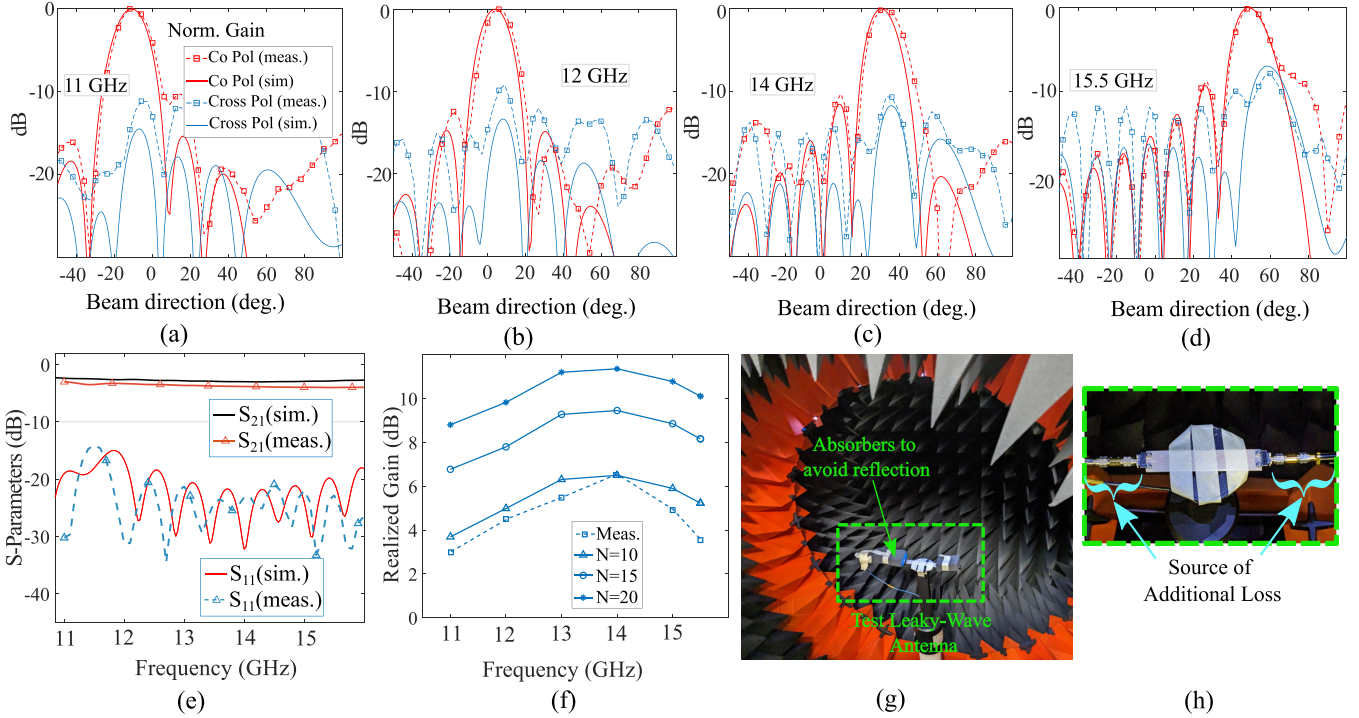


Fig. 14. Measurements in the Ku-band where the antenna is linearly polarized. Measured and simulated normalized radiation patterns of the fabricated antenna in the H-plane at (a) 11, (b) 12, (c) 14, and (d) 15.5 GHz. (e) Simulated and measured S-parameters. (f) Realized gain in the Ku-band with different numbers of unit cells obtained through full-wave simulations. (g) Experimental setup for the measurement in the Ku-band. (h) Additional connectors required to connect the antenna to the ports of VNA.

simulations. This is due to the fact that there is reflection from the connector due to a very tilted beam in the H-plane. The 3-dB beamwidth of the antenna is about 10° throughout the operational range. The length of the antenna remains compact at $7.67\lambda_0 (= c/f_b)$.

The measured and simulated axial ratios are compared in Fig. 13(e). The realized gain plot and directivity of the reconfigurable fan-beam radiation pattern in the H-plane are also shown in Fig. 13(e). The measured S-parameters show that the reflection coefficient remains below -10 dB for the

TABLE III
COMPARISON WITH OTHER SCANNING LWAS OPERATING IN SIMILAR FREQUENCY RANGES

Ref	Antenna Type	Frequency BW	Scanning Range	Realized Gain (dB)	Rel. Permittivity (ϵ_r)	Pol.
[29]	Microstrip with metallized vias	20 GHz to 29 GHz	95° (-50° to 45°)	Approx. 10	6.15	Circular
[10]	Microstrip with metallized vias	9.8 GHz to 15 GHz	72° (-52° to 20°)	10.0–15.1	2.2	Circular
[43]	SIW	26 GHz to 43 GHz	70° (-40° to 30°)	13.4–15	3.0	Linear
[28]	SIW	23 GHz to 25 GHz	30° (-15° to 15°)	15	3.66	Circular
[44]	SIW	10 GHz to 14 GHz	65° (-40° to 25°)	5.1–13	3.0	Circular
[31]	Microstrip	20.6 GHz to 24.6 GHz	85° (-40° to 45°)	9.8–13	3.0	Linear
This Work – K-band	Microstrip	19.4 GHz to 27.5 GHz	72° (-42° to 30°)	7–13	3.0	Circular
This Work – Ku-band	Microstrip	11 GHz to 15.5 GHz	75°(-15° to 60°)	3.1–6	3.0	Linear

operational range. The simulated radiation efficiency (η_{rad}) of the LWA (as defined in [27]) in this band varies from 0.5 to 0.75. The measured total radiation efficiency (η_{tot}) varies from 0.45 to 0.72 as shown in Fig. 13(f). The total radiation efficiency contains the effect of mismatch loss due to matching circuit [45]. The total radiation efficiency of the antenna is obtained by dividing the measured realized gain with directivity [4], [46].

C. Linearly Polarized Radiation in Ku-Band

The antenna is linearly polarized in the Ku-band (11–15.5 GHz) and the radiation occurs due to the $n = -1$ spatial harmonic. The simulated and measured realized gains are shown in Fig. 14(a)–(d). The antenna scanning range is of -15° to 60° . The 3-dB beamwidth of the antenna is less than 17° throughout the operational range. The measured reflection coefficient is below -10 dB in the operating frequency range as shown in Fig. 14(e).

Measurement is performed using MVG Starlab measurement system at IETR, as shown in Fig. 14(g). The antenna is fixed on the platform using tapes to avoid displacement. To avoid the elevated sidelobe levels at high tilted angles, absorbers are added at the either end.

It has to be noted that the antenna has been designed to operate in the K-band and Ku-band, with a special attention to the performance in the K-band. As a consequence, the gain in the Ku-band is limited to 6 dB. However, the realized gain can be improved by adding unit cells to the LWA as shown in Fig. 14(f). Another approach is to increase the thickness of the dielectric substrate (Rogers 3003) on which the LWA is designed to improve the realized gain. This approach is discussed in detail in Section IV-E. It is also important to note that the realized gain in the Ku-band of the antenna is lower by 1–2 dB in the measurements than simulations as shown in Fig. 14(f). This is the effect of the connectors required to properly connect the antenna to the ports of vector network analyzer (VNA) as depicted in Fig. 14(h).

D. Literature Comparison

Table III shows the comparison with the antennas operating in similar frequency ranges along with fabrication technology.

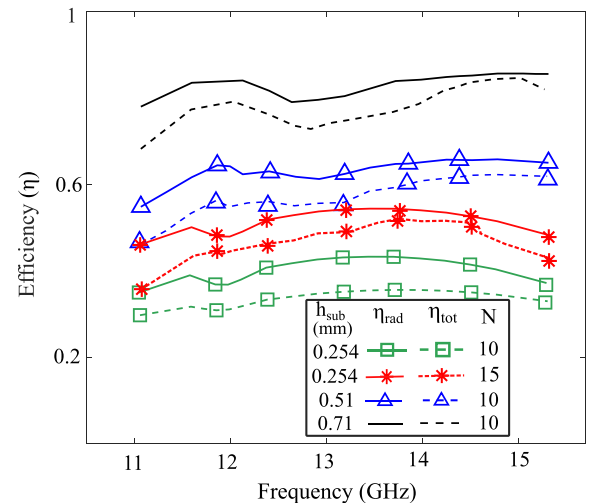


Fig. 15. Efficiency as a function of frequency in the Ku-band for different dielectric (Rogers 3003) thicknesses (h_{sub}) of the LWA keeping all the other dimensions unchanged.

Circularly polarized LWAs operating in the ranges 9.8–15 and 20–29 GHz based on microstrip are reported in [10] and [29]. Both the designs require via-holes, thus increasing the complexity for fabrication compared with the proposed design. The works in [31] and [47] report LWA based on microstrip operating in similar the mm-Wave range; however, they exhibit linear polarization. Composite right left-handed (CRLH)-based structures such as the ones reported in [3], [5], and [48] are extremely sensitive to the dimensions of the slot making them difficult to fabricate with precision at high frequencies.

Meanwhile, the proposed antenna achieves large beam scanning angles with simple meandering microstrips, while maintaining circular polarization. The design can be scaled at lower or higher frequencies very easily without the increase in complexity of fabrication.

E. Improving the Low Gain and Low Efficiency of the Antenna in the Ku-Band

The efficiency and gain of the prototyped LWA in the Ku-band are shown in Figs. 15 and 16, respectively

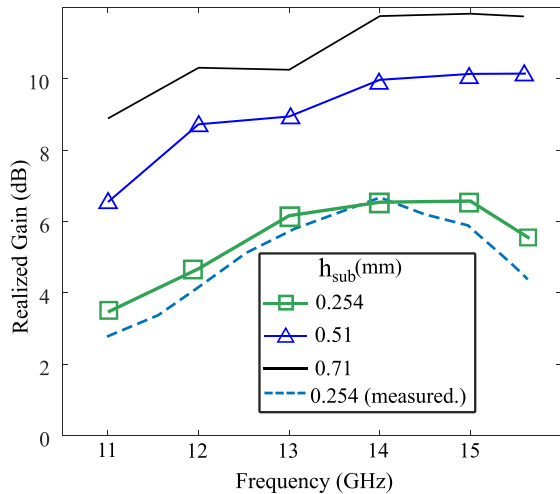


Fig. 16. Increase in realized gain in the Ku-band for different dielectric thicknesses for an LWA comprising $N = 10$ unit cells.

(corresponding to $N = 10$ and substrate thickness of $h_{\text{sub}} = 0.254$ mm). To improve the gain of the antenna in the Ku-band, more than $N = 10$ unit cells can be cascaded as suggested in Section III-C and Fig. 14(f). However, the efficiency of the LWA remains low even with a higher number of unit cells in the Ku-band as shown in Fig. 15 ($N = 15$ and $h_{\text{sub}} = 0.254$ mm). This indicates that the prototyped LWA is inherently a poor radiator in the Ku-band.

To enhance the efficiency and overall performance of the antenna without increasing the number of unit cells in the original LWA (i.e., $N = 10$), one approach is to increase the dielectric substrate thickness while keeping all other dimensions unchanged. This reduces the coupling of the electric fields from the microstrip to the ground while increasing the fringing fields [38] resulting in increased radiation from the mitred corners. This makes the LWA a better radiator in the Ku-band (and K-band as well). Fig. 15 shows the improvement in efficiency when the thickness of substrate is increased while cascading the same number of unit cells as the prototyped LWA ($N = 10$). The realized gain of the LWA also increases as shown in Fig. 16 for the same physical length ($=Np$). Since the increase in thickness is essentially increasing the aperture efficiency resulting in lower aperture length of the antenna, this leads to an increase in the 3-dB beamwidth of the LWA [27]. For the substrate thickness of 0.254, 0.51, and 0.71 mm the 3-dB beamwidth is 17° , 18.7° , and 19.5° , respectively. The antenna retains all the other properties, including the beam scanning with frequency, linear polarization in the Ku-band, and circular polarization in the K-band.

Even though the substrate thickness of 0.254 mm is responsible for a lower efficiency in the Ku-band, this thickness was chosen for the prototype to maximize the bendability of the antenna for on-body applications.

V. CONCLUSION

This article presents a novel approach to designing a compact and single-layer circularly polarized LWA. The approach is based on using the time delay of microstrip line intervals

to achieve circular polarization. The frequency scanning LWA operates as circularly polarized antenna in the K-band and as linearly polarized antenna in the Ku-band. This is possible by the use of spatial harmonics $n = -2$ and $n = -1$, respectively. To improve the band separation and reduce the sidelobes due to unwanted harmonics in the radiation zone, additional meanders have been introduced. The axial ratio remains below 3 dB over large frequency range (19.4–27.5 GHz) in the intended band for circular polarization. This ensures large scanning range from 72° (-42° to 30°). A novel technique to remove OSB is also explained in the work to have continuous scanning through broadside direction.

The proposed antenna does not make use of metallized vias hence significantly reducing the complexity of fabrication while maintaining compact size ($7.67\lambda_0$). The antenna is manufactured on a flexible substrate of Rogers 3003, making it suitable for flexible and conformal purposes at mm-wave frequencies.

REFERENCES

- [1] C. H. Walter, *Traveling Wave Antennas*. New York, NY, USA: McGraw-Hill, 1965.
- [2] C. A. Balanis, *Antenna Theory: Analysis and Design*. Hoboken, NJ, USA: Wiley, Dec. 2015.
- [3] R. Agarwal, R. L. Yadava, and S. Das, "A multilayered SIW-based circularly polarized CRLH leaky wave antenna," *IEEE Trans. Antennas Propag.*, vol. 69, no. 10, pp. 6312–6321, Oct. 2021.
- [4] A. Sarkar and S. Lim, "60 GHz compact larger beam scanning range PCB leaky-wave antenna using HMSIW for millimeter-wave applications," *IEEE Trans. Antennas Propag.*, vol. 68, no. 8, pp. 5816–5826, Aug. 2020.
- [5] M. M. Sabahi, A. A. Heidari, and M. Movahhedi, "A compact CRLH circularly polarized leaky-wave antenna based on substrate-integrated waveguide," *IEEE Trans. Antennas Propag.*, vol. 66, no. 9, pp. 4407–4414, Sep. 2018.
- [6] C. Caloz, T. Itoh, and A. Rennings, "CRLH metamaterial leaky-wave and resonant antennas," *IEEE Antennas Propag. Mag.*, vol. 50, no. 5, pp. 25–39, Oct. 2008.
- [7] J. Liu, X. Tang, Y. Li, and Y. Long, "Substrate integrated waveguide leaky-wave antenna with H-Shaped slots," *IEEE Trans. Antennas Propag.*, vol. 60, no. 8, pp. 3962–3967, Aug. 2012.
- [8] G. P. Carrara, C. L. Zekios, and S. V. Georgakopoulos, "A TM₁₁ high-order mode leaky wave antenna," *IEEE Trans. Antennas Propag.*, vol. 71, no. 1, pp. 119–130, Jan. 2023.
- [9] G. Sacco, O. Caytan, S. Pisa, and H. J. Visser, "Analysis and modelling of rampart line antennas," *IET Microw. Antennas Propag.*, vol. 15, no. 12, pp. 1605–1617, Oct. 2021.
- [10] S. Zhao and Y. Dong, "Circularly polarized beam-steering microstrip leaky-wave antenna based on coplanar polarizers," *IEEE Antennas Wireless Propag. Lett.*, vol. 21, no. 11, pp. 2259–2263, Nov. 2022.
- [11] N. Yang, C. Caloz, and K. Wu, "Full-space scanning periodic phase-reversal leaky-wave antenna," *IEEE Trans. Microw. Theory Techn.*, vol. 58, no. 10, pp. 2619–2632, Oct. 2010.
- [12] J. Duan and L. Zhu, "A transversal single-beam EH₀-mode microstrip leaky-wave antenna on coupled microstrip lines under differential operation," *IEEE Antennas Wireless Propag. Lett.*, vol. 20, no. 4, pp. 592–596, Apr. 2021.
- [13] H. Wang, S. Sun, and X. Xue, "A periodic meandering microstrip line leaky-wave antenna with consistent gain and wide-angle beam scanning," *Int. J. RF Microw. Comput.-Aided Eng.*, vol. 32, no. 7, Jul. 2022, Art. no. e23162.
- [14] J. R. James, P. S. Hall, and C. Wood, *Microstrip Antenna: Theory and Design* (IEE Electromagnetic Waves Series), no. 12. London, U.K.: IET, ch 7, Sec 7.4.1, 1986, pp. 215–218.
- [15] J. L. Volakis, *Antenna Engineering Handbook*, 4th ed. New York, NY, USA: McGraw-Hill, 2007.
- [16] M. R. Rahimi, M. S. Sharawi, and K. Wu, "Higher-order space harmonics in substrate integrated waveguide leaky-wave antennas," *IEEE Trans. Antennas Propag.*, vol. 69, no. 8, pp. 4332–4346, Aug. 2021.

- [17] D.-F. Guan, Q. Zhang, P. You, Z.-B. Yang, Y. Zhou, and S.-W. Yong, "Scanning rate enhancement of leaky-wave antennas using slow-wave substrate integrated waveguide structure," *IEEE Trans. Antennas Propag.*, vol. 66, no. 7, pp. 3747–3751, Jul. 2018.
- [18] P. J. Soh, S. J. Boyes, G. A. E. Vandenbosch, Y. Huang, and S. L. Ooi, "On-body characterization of dual-band all-textile PIFA," *Prog. Electromagn. Res.*, vol. 129, pp. 517–539, 2012.
- [19] P. J. Soh, G. A. E. Vandenbosch, M. Mercuri, and D. M. M.-P. Schreurs, "Wearable wireless health monitoring: Current developments, challenges, and future trends," *IEEE Microw. Mag.*, vol. 16, no. 4, pp. 55–70, May 2015.
- [20] H. Herssens, W. Joseph, and A. Thielens, "A survey of on-body antenna arrays: Future improvements, new designs, and lessons learned," *IEEE Antennas Propag. Mag.*, vol. 65, no. 3, pp. 86–96, Jun. 2023.
- [21] I. V. Soares, P. Vadher, A. K. Skrivervik, G. Sacco, and D. Nikolayev, "Analysis of non-canonical body-conformal arrays with polarization decomposition," in *Proc. 17th Eur. Conf. Antennas Propag. (EuCAP)*, Mar. 2023, pp. 1–5.
- [22] X. Tian, Q. Zeng, D. Nikolayev, and J. S. Ho, "Conformal propagation and near-omnidirectional radiation with surface plasmonic clothing," *IEEE Trans. Antennas Propag.*, vol. 68, no. 11, pp. 7309–7319, Nov. 2020.
- [23] J. Hasch, E. Topak, R. Schnabel, T. Zwick, R. Weigel, and C. Waldschmidt, "Millimeter-wave technology for automotive radar sensors in the 77 GHz frequency band," *IEEE Trans. Microw. Theory Techn.*, vol. 60, no. 3, pp. 845–860, Mar. 2012.
- [24] J. C. G. Matthews and G. Pettitt, "Development of flexible, wearable antennas," in *Proc. 3rd Eur. Conf. Antennas Propag.*, Mar. 2009, pp. 273–277.
- [25] P. Vadher, G. Sacco, and D. Nikolayev, "On-body V-band leaky-wave antenna for navigation and safety applications," in *Proc. IEEE Microw. Antennas, Propag. Conf. (MAPCON)*, Dec. 2022, pp. 1741–1746.
- [26] R. Henry and M. Okoniewski, "A broadside-scanning half-mode substrate integrated waveguide periodic leaky-wave antenna," *IEEE Antennas Wireless Propag. Lett.*, vol. 13, pp. 1429–1432, 2014.
- [27] D. R. Jackson and A. A. Oliner, "Leaky-wave antennas," in *Modern Antenna Handbook*. Hoboken, NJ, USA: Wiley, 2008, pp. 325–367.
- [28] S. Otto, Z. Chen, A. Al-Bassam, A. Rennings, K. Solbach, and C. Caloz, "Circular polarization of periodic leaky-wave antennas with axial asymmetry: Theoretical proof and experimental demonstration," *IEEE Trans. Antennas Propag.*, vol. 62, no. 4, pp. 1817–1829, Apr. 2014.
- [29] M. H. Rahmani and D. Deslandes, "Backward to forward scanning periodic leaky-wave antenna with wide scanning range," *IEEE Trans. Antennas Propag.*, vol. 65, no. 7, pp. 3326–3335, Jul. 2017.
- [30] S. Paulotto, P. Baccarelli, F. Frezza, and D. R. Jackson, "A novel technique for open-stopband suppression in 1-D periodic printed leaky-wave antennas," *IEEE Trans. Antennas Propag.*, vol. 57, no. 7, pp. 1894–1906, Jul. 2009.
- [31] P. Vadher, G. Sacco, and D. Nikolayev, "Higher spatial harmonic leaky wave antenna design based on meandering microstrips," in *Proc. 17th Eur. Conf. Antennas Propag. (EuCAP)*, Florence, Italy, Mar. 2023, pp. 1–4.
- [32] S. Cheng, Y. Li, Z. Liang, S. Zheng, and Y. Long, "An approximate circuit model to analyze microstrip rampart line in OSB suppressing," *IEEE Access*, vol. 7, pp. 90412–90417, 2019.
- [33] S.-L. Chen, D. K. Karmokar, Z. Li, P.-Y. Qin, R. W. Ziolkowski, and Y. J. Guo, "Circular-polarized substrate-integrated-waveguide leaky-wave antenna with wide-angle and consistent-gain continuous beam scanning," *IEEE Trans. Antennas Propag.*, vol. 67, no. 7, pp. 4418–4428, Jul. 2019.
- [34] C. Wood, "Curved microstrip lines as compact wideband circularly polarised antennas," *IEE J. Microw., Opt. Acoust.*, vol. 3, no. 1, p. 5, 1979.
- [35] D. R. Jackson, C. Caloz, and T. Itoh, "Leaky-wave antennas," *Proc. IEEE*, vol. 100, pp. 2194–2206, 2011.
- [36] R. E. Collin and F. J. Zucker, *Antenna Theory*, vol. 2. New York, NY, USA: McGraw-Hill, 1969, ch. 19–20.
- [37] A. Ishimaru, *Electromagnetic Wave Propagation, Radiation, and Scattering: From Fundamentals to Applications* (The IEEE Press Series on Electromagnetic Wave Theory), 2nd ed. Piscataway, NJ, USA: IEEE Press, 2017.
- [38] D. M. Pozar, *Microwave Engineering*, 4th ed. Hoboken, NJ, USA: Wiley, Nov. 2011.
- [39] M. N. O. Sadiku, S. M. Musa, and S. R. Nelatury, "Comparison of dispersion formulas for microstrip lines," in *Proc. IEEE SoutheastCon*, Mar. 2004, pp. 378–382.
- [40] R. J. P. Douville and D. S. James, "Experimental study of symmetric microstrip bends and their compensation," *IEEE Trans. Microw. Theory Techn.*, vol. MTT-26, no. 3, pp. 175–182, Mar. 1978.
- [41] P. Silvester and P. Benedek, "Microstrip discontinuity capacitances for right-angle bends, T junctions, and crossings," *IEEE Trans. Microw. Theory Techn.*, vol. MTT-21, no. 5, pp. 341–346, May 1973.
- [42] P. Anders and F. Arndt, "Microstrip discontinuity capacitances and inductances for double steps, mitered bends with arbitrary angle, and asymmetric right-angle bends," *IEEE Trans. Microw. Theory Techn.*, vol. MTT-28, no. 11, pp. 1213–1217, Nov. 1980.
- [43] Y. Geng, J. Wang, Y. Li, Z. Li, M. Chen, and Z. Zhang, "A Ka-band leaky-wave antenna array with stable gains based on HMSIW structure," *IEEE Antennas Wireless Propag. Lett.*, vol. 21, no. 8, pp. 1597–1601, Aug. 2022.
- [44] Y.-L. Lyu, F.-Y. Meng, G.-H. Yang, D. Erni, Q. Wu, and K. Wu, "Periodic SIW leaky-wave antenna with large circularly polarized beam scanning range," *IEEE Antennas Wireless Propag. Lett.*, vol. 16, pp. 2493–2496, 2017.
- [45] H. V. Nguyen, S. Abielmona, and C. Caloz, "Highly efficient leaky-wave antenna array using a power-recycling series feeding network," *IEEE Antennas Wireless Propag. Lett.*, vol. 8, pp. 441–444, 2009.
- [46] E. Massoni, M. Bozzi, and K. Wu, "Increasing efficiency of leaky-wave antenna by using substrate integrated slab waveguide," *IEEE Antennas Wireless Propag. Lett.*, vol. 18, no. 8, pp. 1596–1600, Aug. 2019.
- [47] Y.-L. Lyu, F.-Y. Meng, G.-H. Yang, P.-Y. Wang, Q. Wu, and K. Wu, "Periodic leaky-wave antenna based on complementary pair of radiation elements," *IEEE Trans. Antennas Propag.*, vol. 66, no. 9, pp. 4503–4515, Sep. 2018.
- [48] Y. D. Dong and T. Itoh, "Composite right/left-handed substrate integrated waveguide and half-mode substrate integrated waveguide," in *IEEE MTT-S Int. Microw. Symp. Dig.*, Jun. 2009, pp. 49–52.